

The Modular Aerial Sensing System

W. KENDALL MELVILLE, LUC LENAIN, DANIEL R. CAYAN, AND MATI KAHRU

Scripps Institution of Oceanography, University of California, San Diego, La Jolla, California

JAN P. KLEISSL AND P. F. LINDEN*

Department of Mechanical and Aerospace Engineering, University of California, San Diego, La Jolla, California

NICHOLAS M. STATOM

Scripps Institution of Oceanography, University of California, San Diego, La Jolla, California

(Manuscript received 14 April 2015, in final form 15 October 2015)

ABSTRACT

Satellite remote sensing has enabled remarkable progress in the ocean, earth, atmospheric, and environmental sciences through its ability to provide global coverage with ever-increasing spatial resolution. While exceptions exist for geostationary ocean color satellites, the temporal coverage of low-Earth-orbiting satellites is not optimal for oceanographic processes that evolve over time scales of hours to days. In hydrology, time scales can range from hours for flash floods, to days for snowfall, to months for the snowmelt into river systems. On even smaller scales, remote sensing of the built environment requires a building-resolving resolution of a few meters or better. For this broad range of phenomena, satellite data need to be supplemented with higher-resolution airborne data that are not tied to the strict schedule of a satellite orbit. To address some of these needs, a novel, portable, high-resolution airborne topographic lidar with video, infrared, and hyperspectral imaging systems was integrated. The system is coupled to a highly accurate GPS-aided inertial measurement unit (GPS IMU), permitting airborne measurements of the sea surface displacement, temperature, and kinematics with swath widths of up to 800 m under the aircraft, and horizontal spatial resolution as low as 0.2 m. These data are used to measure ocean waves, currents, Stokes drift, sea surface height (SSH), ocean transport and dispersion, and biological activity. Hydrological and terrestrial applications include measurements of snow cover and the built environment. This paper describes the system, its performance, and present results from recent oceanographic, hydrological, and terrestrial measurements.

1. Introduction

Over the last few decades, satellite remote sensing has enabled remarkable progress in the ocean, earth, atmospheric, and environmental sciences through its

ability to provide global coverage with ever-increasing spatial resolution down to the order of tens of meters for some instruments, and 1 m and less for visible imagery and synthetic aperture radar (SAR). While geostationary satellites can provide high spatial and temporal coverage for ocean color [e.g., the Geostationary Ocean Color Imager (GOCI); [Ryu et al. 2012](#)], the temporal coverage of low-Earth-orbiting satellites is not optimal, with typical repeat cycles of the order of 10 days or more. This sampling frequency may be sufficient to resolve mesoscale ocean processes (e.g., ocean eddies), which may have time scales of a month, but it is not sufficient for ocean processes that respond to atmospheric forcing with time scales of days to a week and other submesoscale ocean processes, especially coastal processes, both physical and biological, and air-sea-land interactions in the coastal zone. In the hydrological

 Denotes Open Access content.

* Current affiliation: Department of Applied Mathematics and Theoretical Physics, University of Cambridge, Cambridge, United Kingdom.

Corresponding author address: W. Kendall Melville, Scripps Institution of Oceanography, University of California, San Diego, 9500 Gilman Dr., La Jolla, CA 92093-0213.
E-mail: kmelville@ucsd.edu

DOI: 10.1175/JTECH-D-15-0067.1

sciences, the time scales can range from hours for flash floods, to days for snowfall on mountain ranges, to months for the snowmelt into the river system. On an even smaller scale, remote sensing of the built environment catalyzes research into more resource-efficient and sustainable cities but requires a building-resolving thermal resolution of a few meters. For this range of phenomena, satellite data are very useful but not optimal, and need to be supplemented with higher-resolution airborne data that are not tied to the strict schedule of a satellite orbit.

Of particular use in airborne remote sensing is lidar along with hyperspectral (including infrared) imagery. Simple lidars measure the first returns of laser pulses from the surface and in the absence of complications—because of, say, vegetation—the data can be interpreted as topographical maps of the surface, including water surfaces. Waveform lidars have a buffer that can store backscatter data over some time-enabling interpretation of the signal in more complicated situations in which there may be structures or vegetation between the first return pulse (e.g., the top of the trees, the top of a power line) and the last (e.g., the ground). In an oceanographic setting, waveform lidars can resolve aerosols and spray above the ocean surface (L. Lenain and W. K. Melville 2015, unpublished manuscript). When combined with hyperspectral/IR imagery, lidar can provide both topography and measures of biological productivity, land use, hydrological variables, and radiative properties based on the hyperspectral/IR image (Lee et al. 2015; Vierling et al. 2008).

With the growing interest in understanding air–sea interaction, upper-ocean dynamics, and thermodynamics, increasing emphasis has been placed on sub-mesoscale and smaller-scale ocean processes. In parallel there has been a growing awareness that air–sea fluxes, many of which are parameterized just on wind speed, must also depend on surface-wave processes, whether it is momentum flux (drag), heat flux, or mass flux—the last of which includes gas transfer by entrained air, and marine spray and aerosol generation by wave breaking. In general, the only way wave effects can drop out of the parameterization is by considering near-asymptotic states of the wave field like “full development,” which is normally not the case (Hanley et al. 2010).

Langmuir turbulence (LT) [or Langmuir circulation (LC)] has been shown to be an important component of upper-ocean (mixed layer) dynamics, entrainment, and mixing. The dynamics of LT depends on a vortex force $\mathbf{u}_s \times \boldsymbol{\omega}$, where \mathbf{u}_s is the Stokes drift, the wave contribution to the Lagrangian mean velocity, and $\boldsymbol{\omega}$ is the vorticity of the near-surface current. Computing the Stokes drift depends on the directional spectrum of the wave field in space and time.

While mesoscale processes may be well correlated with the geostrophic currents inferred from the sea surface height (SSH) measured by satellite altimetry on a typical 10-day repeat cycle, as we move to sub-mesoscale and coastal processes, improved spatial and temporal resolution is required. For example, with the 2-km-spatial-resolution requirement and 500-m goal of the Surface Water and Ocean Topography (SWOT) altimetry mission (<https://swot.jpl.nasa.gov/>), the surface wave field will become of more significance for the kinematics and dynamics inferred by the altimeter, and for the sea-state bias corrections since the wave field correlates with the submesoscale dynamics through wave–current interaction. As the oceanographic community moves more and more into this submesoscale regime of ocean dynamics, some of these needs can be met by the use of airborne (suborbital) ocean remote sensing using lidar for the measurement of ocean topography from mesoscales of $O(100\text{--}1000)$ km to gravity–capillary waves of wavelengths $O(1\text{--}10)$ cm. Thus, airborne remote sensing can be used in the pre-launch and calibration–validation phases and to supplement the science goals of missions like SWOT.

In this paper we describe the Modular Aerial Sensing System (MASS)¹, which is built around a waveform scanning lidar and includes a high-resolution camera, infrared and hyperspectral imaging systems, and a very precise GPS-aided inertial measurement unit (GPS IMU), which permits the data to be referenced to an Earth frame. We then go on to present the initial results of using the system in experiments off the coast of California, the Carolinas, and the Gulf of Mexico. We also show a terrestrial use of the lidar in measuring the snow cover in the Sierra Nevada, an important natural seasonal reservoir for California’s water supply and, finally, an example of measuring the built environment of a university campus.

2. Modular Aerial Sensing System

The MASS is shown during bench top testing in Fig. 1a along with the aircraft used for the 2011 Gulf of Mexico experiment, a Partenavia P.68 light twin engine, which is shown in Fig. 1b. The MASS components, weight, and power requirements are given in Table 1, demonstrating that the system is small enough and efficient enough to also be flown in single-engine aircraft for missions in which the limitations of such aircraft are not a safety issue (e.g., very nearshore coastal oceanography).

¹ A much earlier, simpler version of MASS was flown on a Long-EZ aircraft for wave and breaking measurements (Melville and Matusov 2002).

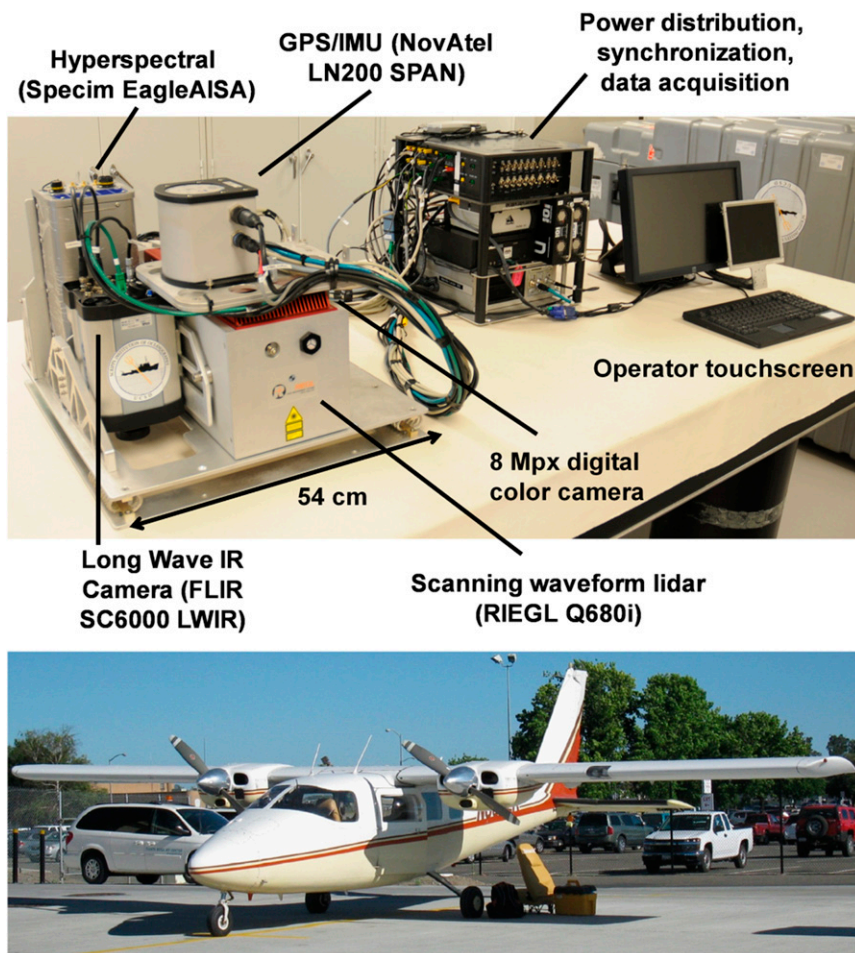


FIG. 1. (top) MASS at the Air–Sea Interaction Laboratory at Scripps Institution of Oceanography prior to a deployment in the Gulf of Mexico in October 2011. (bottom) The instrument package was installed on a Partenavia P.68 aircraft for the Gulf of Mexico experiment, 17–31 October 2011. The airborne system includes a scanning waveform lidar, longwave infrared (LWIR) camera, SST sensor, visible high-resolution camera, hyperspectral (VNIR) imager, and a GPS IMU system (see [Table 1](#)).

The core of the system for ocean wave and SSH measurements is a Q680i, 1550-nm waveform scanning elastic topographic lidar (Riegl) that has a maximum pulse repetition rate of 400 kHz, has a maximum $\pm 30^\circ$ raster scan rate of 200 Hz, and has been used at altitudes of up to 1000 m with good returns for surface-wave measurements. The theoretical swath width over water is typically proportional to the altitude of the aircraft, and its effective width is also dependent on the wind speed and sea state, as shown in [Table 2](#) (see also [Reineman et al. 2009](#)).

The 14-bit, 640×512 quantum well infrared photodetector (QWIP) FLIR SC6000 infrared camera operates up to a 126-Hz frame rate in the 8.0–9.2- μm band, with a temperature range of -10° to 80°C , an integration time of 10 ms, and a stated rms noise level below 35 mK. In our oceanographic applications, it is used to measure

the ocean surface temperature field, including modulations and gradients due to fronts, LT, and wave breaking ([Sutherland and Melville 2013](#)). It is also used along with image processing techniques [optical flow and particle imaging velocimetry (PIV)] to measure surface currents by the advection of the surface temperature patterns.

The hyperspectral camera is a push-broom system (SPECIM AisaEAGLE) operating in the 400–990-nm range [visible to near IR (VNIR)], with 1.25-nm native spectral resolution and a 944-pixel swath resolution, for a swath width of approximately 570 m at 900 m (3000 ft) MSL using a 18.57-mm lens, corresponding to a 0.6-m cross-track spatial resolution. The imager is used to measure biological activity (e.g., red tides, chlorophyll-*a*) and to measure the dispersion of dyes in the ocean. To produce calibrated radiance values [$\text{mW} (\text{cm}^2 \text{sr} \mu\text{m})^{-1}$],

TABLE 1. Primary instrumentation of MASS and its application in an oceanic environment. The weight is 120 kg total (including acquisition rack); 79 kg without hyperspectral imager. The power requirements are 600 W total; 400 W without hyperspectral imager.

Instrumentation	Measurement
Scanning waveform lidar (Riegl Q680i)	Surface waves, surface slope, directional wave spectra (vertical accuracy ~2–3 cm per point)
LWIR camera (QWIP FLIR SC6000)	Ocean surface processes, wave kinematics and breaking, frontal processes
High-resolution video (Jai Pulnix AB-800CL)	Ocean surface processes, wave kinematics and breaking, frontal processes
Hyperspectral camera (Specim AisaEAGLE)	Ocean surface and biogeochemical processes
GPS IMU (Novatel SPAN LN200)	Georeferencing, trajectory

measurements of incoming downwelling radiation are collected using a fiber-optic downwelling irradiance sensor (FODIS) placed atop the fuselage of the aircraft and synchronized with the hyperpectral camera. The camera system (hyperspectral and FODIS sensor) was calibrated at the SpecTIR facility prior to installation on the aircraft. The resulting calibration provides data that are within $\pm 5\%$ of absolute radiance, with central wavelength locations within 0.5-nm accuracy. The noise reference value, collected at the end of each flight line, is removed from the imagery prior to radiance calibration.

The Jai Pulnix AB-800CL is an 8.1-Mpx (3296×2472) color/black and white (24/12 bit) video camera that operates at a frame rate up to 17 Hz and is used to provide reference imagery in addition to visible imagery of the kinematics of whitecaps (Kleiss and Melville 2010, 2011; Melville and Matusov 2002; Sutherland and Melville 2013).

The Novatel SPAN LN200 is a very accurate GPS IMU system combining GPS technology with an IMU using fiber-optic gyros and solid-state accelerometers to provide position and attitude data at up to 200 Hz. After differential GPS processing using Waypoint Inertial Explorer software, the stated accuracy for position is 0.01 m horizontal and 0.015 m (vertical), and attitude accuracies of 0.005° , 0.005° , and 0.008° for roll, pitch, and heading, respectively.

As stated above the power requirements (600 W) and weight (120 kg) of the system are small enough to be operated from a small single-engine aircraft in terrestrial or nearshore applications. For reasons of flight safety, we use a light-twin-engine aircraft, a Partenavia P.68, when flying offshore. Figure 2 shows MASS installed in a P.68 aircraft during the Office of Naval Research (ONR) Inlets and Rivers Mouth Dynamics Departmental Research Initiative (RIVET DRI) field effort (New River Inlet, North Carolina) in May 2012. With an endurance of 4.5–6 h² at a cruise speed of 120 kt (1 kt = 0.51 m s^{-1}) and a typical airspeed of 100 kt during MASS data acquisition, this and similar aircraft can

provide significant time and aerial coverage while on station.

Prior to each field campaign, a calibration–validation flight is conducted to characterize and minimize boresight errors due to the misalignment between the GPS IMU system and the lidar, IR, visible, and hyperspectral cameras. The boresight flight consists of several overlapping, opposing direction, and crossing flight lines over an area with a high concentration of houses with flat-surfaced, angled roofs. We use an automated detection tool, part of the Riegl RiProcess and RiAnalyze software suite to iteratively compute the boresight angles and level arm (x , y , z directions) that minimize misalignment errors of a distribution of flat surfaces collected from flight lines of various headings and directions.

3. Oceanographic and coastal applications

a. Directional measurements of the ocean surface wave field at high wavenumber

The high pulse repetition and line-scanning rates of the Riegl Q680i lidar with a single-pulse range accuracy of 2 cm, when compared to the previous systems used (Huang et al. 2012; Reineman et al. 2009; Romero and Melville 2010a), lead to very high-resolution directional surface-wave measurements. An example of a directional spectrum from a flight off San Clemente Island conducted in November 2013 is shown in Fig. 3b along with the azimuthally integrated omnidirectional spectrum in Fig. 3a. The latter clearly shows the separation of the spectral slopes into -2.5 and -3 regions, consistent with wave dynamics and modeling (the -2.5 slope is consistent with an “equilibrium wave spectrum,” for which there is, at leading order, a dynamical balance between wind input, nonlinear wave–wave interactions, and dissipation, mainly due to breaking; this evolves into the -3 slope, consistent with the “saturation spectrum” in which the primary balance is between wind input and dissipation; Banner 1990; Phillips 1985; Romero and Melville 2010a,b; Romero et al. 2012). These data down to wavelengths of approximately 60 cm were acquired at a flight altitude of approximately 200 m.

² Actual endurance can vary based on the number of passengers and P.68 model.

TABLE 2. Lidar system nominal performances. These values require the lidar to be set at a 400-kHz pulse repetition rate. The aircraft speed was set to 100 kt.

Altitude ASL/AGL (m)	Max swath width (m)	Optimal spatial resolution along/cross ^a (m)	Beam footprint [diameter (m)]	Horizontal spatial resolution (m)
100	116	0.25/0.08	0.05	0.04
300	352	0.25/0.25	0.15	0.10
500	580	0.32/0.32	0.25	0.16
1000	1161	0.45/0.45	0.5	0.32
1500	1730	0.55/0.55	0.75	0.48

^aThe “optimal” spatial resolution is obtained by reducing the lidar scanning rate to get comparable along- and cross-track spatial resolution.

To leading order, the Stokes drift from the directional spectrum of Fig. 3 can be inferred from

$$\mathbf{u}_s(z) = g \int_{\mathbf{k}} S(\mathbf{k}) \frac{\mathbf{k}}{\omega} \left[\frac{2k \cosh 2k(z+h)}{\sinh 2kh} \right] d\mathbf{k}, \quad (1)$$

where the wavenumber $k = |\mathbf{k}|$ is in the range $[k_l \leq k \leq k_c]$, z is the vertical coordinate, h is the water depth, ω is the radian frequency computed from the linear dispersion relationship, and $S(\mathbf{k})$ is the wavenumber directional spectrum of the surface displacement (Kenyon 1969). Note that, in general, the wave spectrum is not symmetric relative to one direction, and that the exponential structure of the orbital motion and Stokes drift in the vertical means that the near-surface structure and direction of the Stokes drift may often be dominated by the higher wavenumbers. This places particular emphasis on our ability to measure the

high-wavenumber part of the spectrum. This is illustrated in Fig. 4, where the differences in Stokes drift inferred by the directional spectrum in Fig. 3 when the high-wavenumber cutoff k_c varies from 10 to 0.05 rad m^{-1} (wavelength λ ranging from 0.6 to 125 m) are shown.

MASS also includes a collocated, synchronized high-resolution infrared and visible video, providing the rare ability to couple the evolution of the wave field with surface kinematics and breaking. Figure 5 shows sample georeferenced images of a breaking wave in the visible and infrared (8–9.2 μm) bands collected during a flight in the Gulf of Mexico on 18 October 2011, shortly after the passage of a cold front. The wind speed measured at a nearby NDBC buoy (station 42040) was 12 m s^{-1} with a significant wave height H_s of 3.1 m. Note that the foam is colder (blue) due to rapid cooling ($T_w - T_a \approx 8^\circ\text{C}$, where T_w is the water temperature and T_a is the atmospheric temperature collected at the nearby NDBC



FIG. 2. MASS installed on a Partenavia P.68 aircraft during the RIVET experiment, New River Inlet, in May 2012. (left) Operator in-flight display, (top right) MASS installed in the P.68, and (bottom right) view of MASS from below the aircraft.

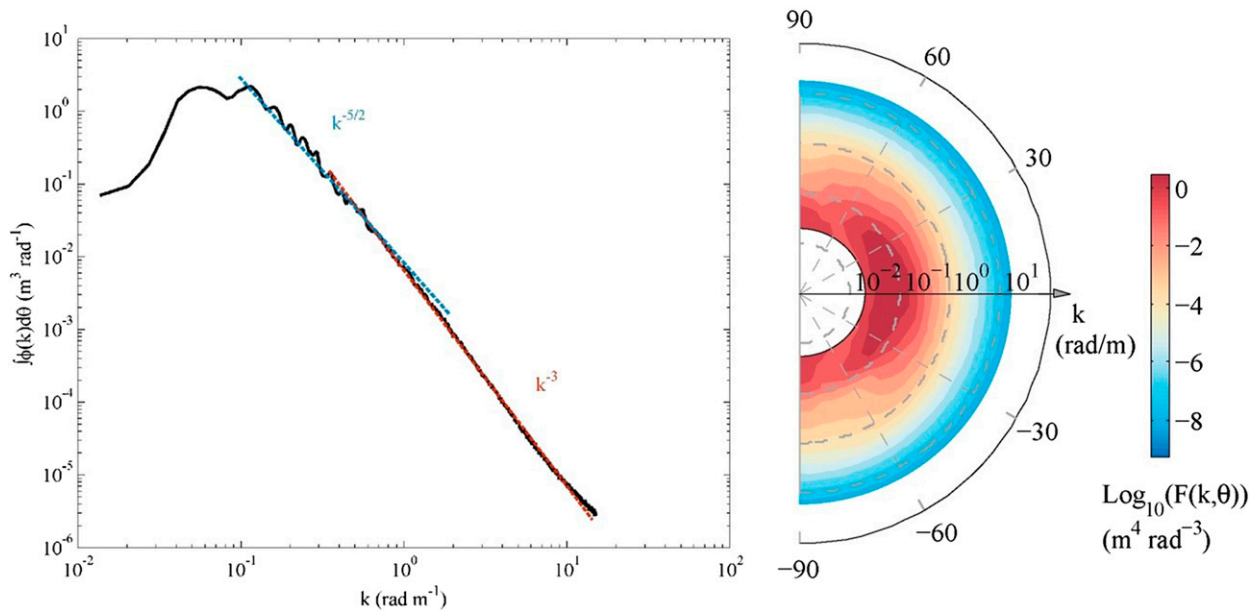


FIG. 3. (right) Directional wavenumber spectrum from the sea surface topography recorded at 150 m MSL using MASS on 15 Nov 2013 off San Clemente Island during the ONR Southern California 2013 (SOCAL2013) experiment at 2008 UTC. These data give spectra down to wavelengths of 0.5 m. (left) Corresponding omnidirectional wavenumber spectrum. Note the $-5/2$ and -3 spectral slopes, and the almost three-decade bandwidth of the data.

buoy), while the active breaker is warmer (red) by disrupting the surface cool skin layer and bringing warmer water from below. Also shown is a perspective view of the sea surface elevation for the same breaking wave color-coded for World Geodetic System 1984 (WGS84) datum height. The lower panel shows the profile of the transect across the breaking wave (A–B) marked in the georeferenced visible image.

b. The Gulf of Mexico experiment

From 17 to 31 October 2011, we had the opportunity to conduct airborne measurements using MASS and the aircraft shown in Fig. 1 to study wave–current interaction across the northern edge of the Loop Current in the Gulf of Mexico: the Gulf of Mexico 2011 experiment (GoM2011). Flight operations were based at Jack Edwards Airport, Gulf Shores, Alabama (30° – 17.378333° N/ 087° – 40.306667° W). During that period there were several satellite altimeter overpasses in close proximity to our base, and we took the opportunity to conduct flights along one satellite track to “coincide” with the satellite. Since an aircraft leg along this track lasted approximately 1–1.5 h, coincident here means within ± 0.5 – 0.75 h.

Figure 6 shows the *Jason-1* descending track and aircraft track that was flown on 30 October 2011, on a bathymetric map of the northeastern Gulf of Mexico at approximately 4-km resolution (NASA 2008). The second panel of the figure, showing sea surface temperature (SST) collected from the *Terra* satellite (NASA 2014)

10 h prior to the flight and the *Jason-1* overflight, also shows that the northern edge of warmer water of the Loop Current was approximately 200 km from base.

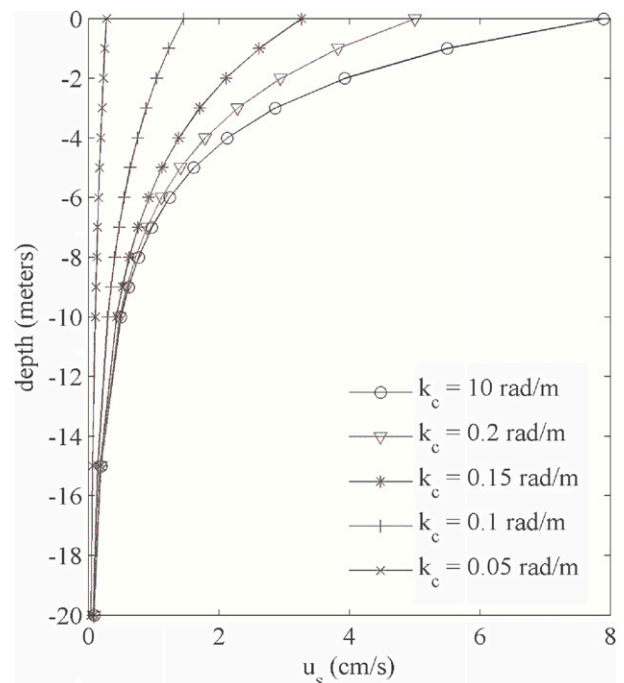


FIG. 4. Evolution of magnitude of the Stokes drift profile computed from the directional wavenumber spectrum from the sea surface topography shown in Fig. 3 for a range of cutoff wavenumbers k_c . Note the sensitivity to the cutoff in the upper 10 m.

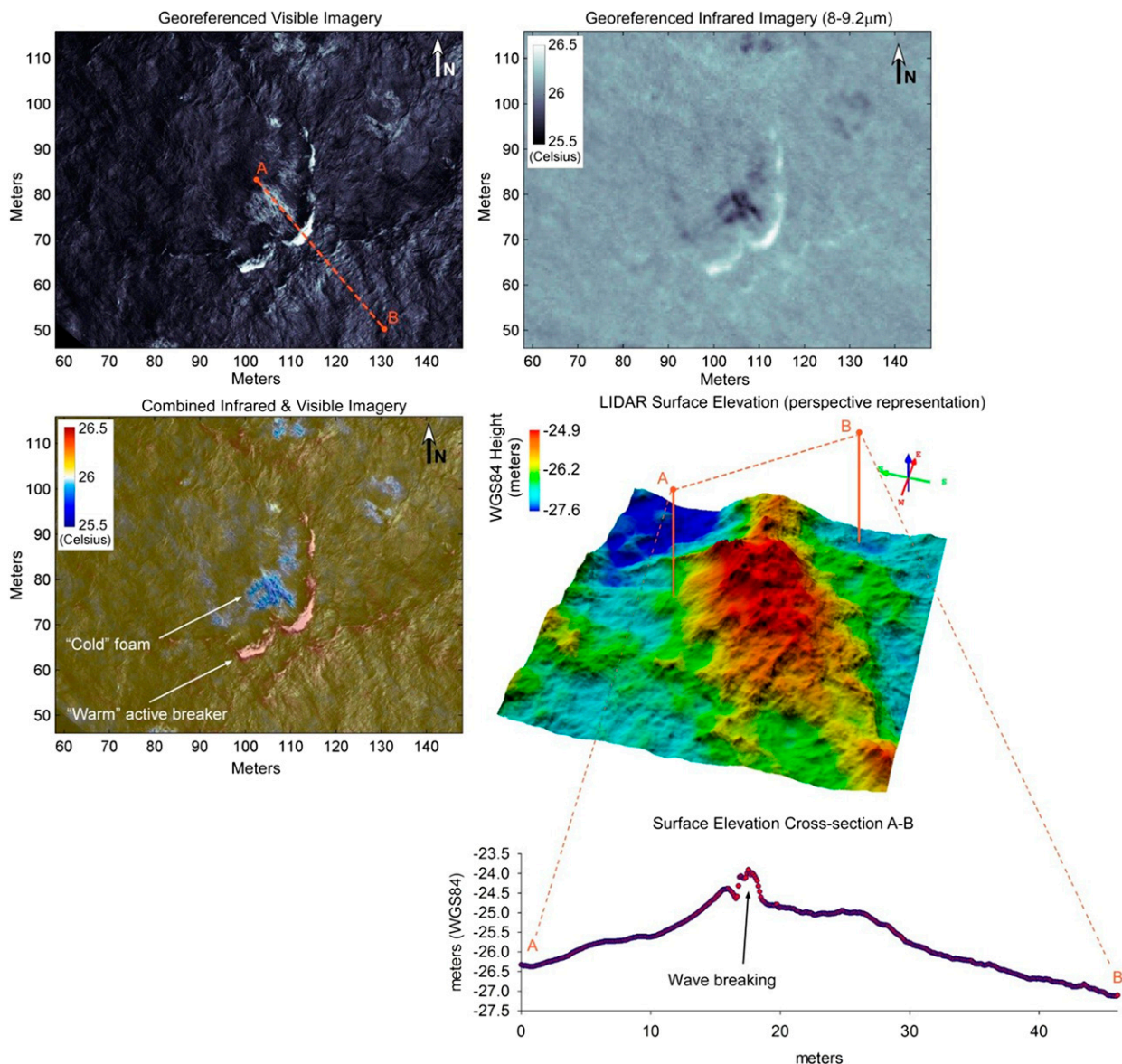


FIG. 5. Sample georeferenced images of a breaking wave in the (top left) visible and (top right) infrared (8–9.2 μm) bands during GoM2011. (bottom left) Note that the foam is colder (blue) due to rapid cooling ($T_{\text{water}} - T_{\text{atm}} \approx 8^{\circ}\text{C}$), while the active breaker is warmer (red), disrupting the surface skin layer and bringing warmer water from below. (bottom right) Also shown is a perspective view of the (top) sea surface elevation for the same breaking wave color-coded for WGS84 height; (bottom) the profile of the transect A–B marked in the georeferenced visible image.

With a round-trip transit of approximately 2 h from Jack Edwards Airport, this left approximately 2.5 h on station in the vicinity of the current boundary.

c. Surface-wave processes and modulations across the Loop Current front

As shown in Fig. 6, the southern end of the flight track on 30 October 2011 extends into the warmer waters of the Loop Current with the Loop Current boundary at approximately 28.1°N.

During this flight the dominant wind waves were propagating toward the southwest, thus meeting an opposing current near the northern boundary of the Loop Current. The opposing current can be assumed from the general structure and dynamics of the current; however, the MASS infrared imager presents an opportunity to actually measure the current, assuming the temperature patterns on the surface are coherent over a sufficiently long time Δt for their displacement to be measured. Using optical flow techniques (Liu 2009) to track the

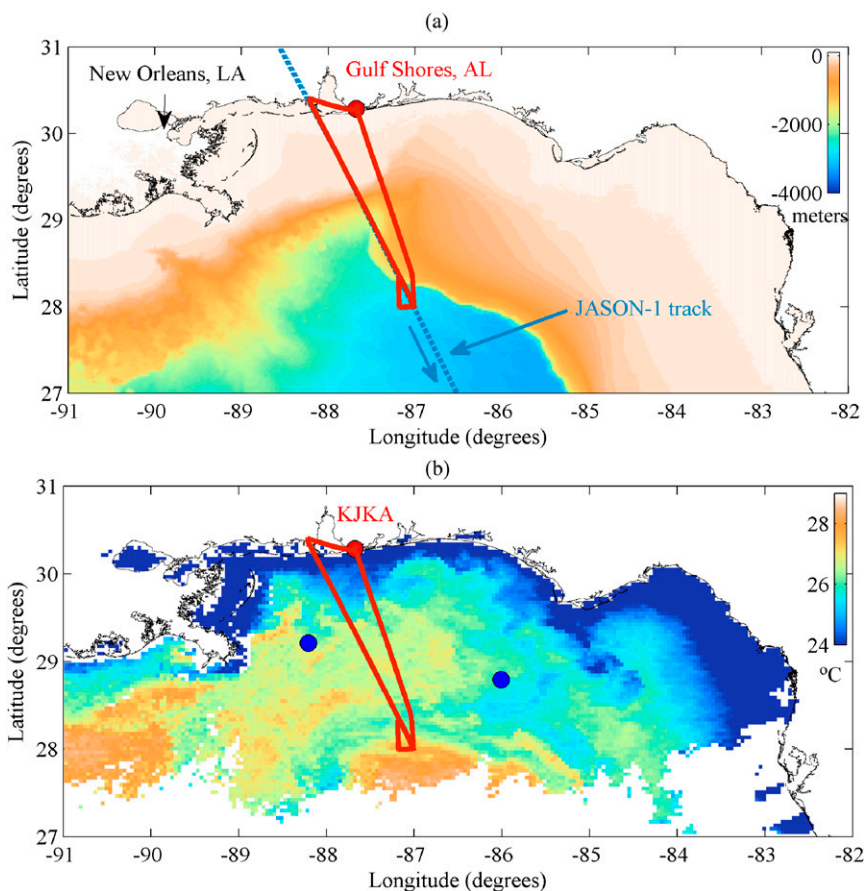


FIG. 6. Map of the northern Gulf of Mexico showing backgrounds of (a) bathymetry and (b) SST estimated from *Terra* level 3 daily product ($^{\circ}\text{C}$) on 30 Oct 2011, 10 h prior to the airborne survey conducted the same day, with the aircraft flight track for that day shown in both images in red. Note that in (a) the *Jason-1* altimeter ground track was also flown by the aircraft that day, permitting a direct comparison of the lidar-measured SSH with the *Jason-1* measurements, coincident within ± 1.5 h. The blue dots in (b) represent the closest NDBC buoy equipped with wave and atmospheric instrumentation operational during the field study.

temperature patterns at the surface of the ocean over Δt in the range of 3–7 s, depending on flight altitude, horizontal surface velocities were measured along the flight track and are shown in Fig. 7. While we have no direct way of confirming these measurements, they are not inconsistent with independent coupled models of the Gulf of Mexico (B. Cornuelle 2015, personal communication). In that context, it should be noted that while the IR imagery here shows that the thermal surface boundary of the current is very sharp over scales of $O(10)$ m, the available regional numerical models of the dynamics are resolved at scales of $O(1)$ km.

From geometrical optics and wave action conservation (Mei et al. 2005), under these conditions we would expect to see an increase in wave amplitude and slope as the waves propagate through the gradient in the current. The SST measured along track and across the Loop Current boundary is shown, along with the

omnidirectional wave spectra color-coded by the temperature. The spectral density near the peak of the spectrum increases by 50%–70% as the waves propagate southwestward into the opposing current (i.e., from cold to warmer water), while the significant wave height (SWH) in this region increases by 20%–25% (see the vertical arrow in Fig. 12), qualitatively consistent with the theory.

The steepening of the waves due to wave–current interaction can lead to wave breaking, the kinematics and statistics of which have been measured using visible imagery from aircraft (Kleiss and Melville 2010, 2011; Melville and Matusov 2002; Romero et al. 2012) and from the Research Platform (R/P) *Floating Instrument Platform (FLIP)* using both visible and IR imagery (Sutherland and Melville 2013). In GoM2011 MASS was able to measure breaking using a combination of the lidar data with the visible and IR imagery. Figure 5

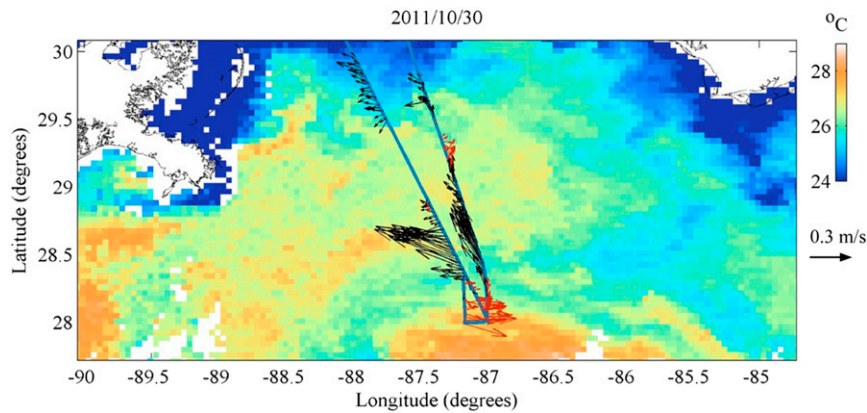


FIG. 7. SST estimated from *Terra* level 3 daily product ($^{\circ}\text{C}$) on 30 Oct 2011, 10 h prior to the airborne survey conducted the same day. The flight track is shown in blue. The average surface velocities derived from the thermal imagery are shown as vectors along the flight track (red, positive easterly velocity; black, negative easterly velocity). Note the sharp change in surface velocities as the aircraft went across the Loop Current front.

shows such an example of a breaker, identifying different thermal structure across the warmer actively breaking front when compared to the cooler decaying foam in the wake of the breaker. It also shows that we can resolve the geometrical structure of the wave during active breaking. In Fig. 8, a composite infrared and visible image shows the enhanced breaking occurring on the warmer side of a temperature front consistent with the steepening of the wave field at the northern edge of the LC.

The local thermal structure and sharpness of a temperature front at the northern edge of the Loop Current shown in Fig. 9a also reveals almost linear streaks approximately aligned with the wind. These structures, which have been seen previously in IR imagery of the sea surface (Marmorino et al. 2008), we believe are the surface signatures of Langmuir turbulence. With complementary in situ data to measure the temperature and velocity structure of the upper mixed layer, airborne measurements of both the wave field (including the

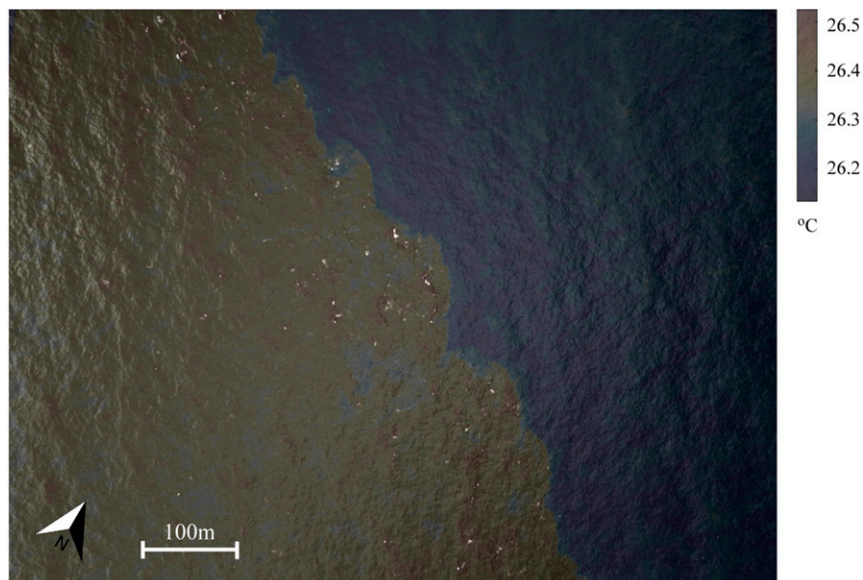


FIG. 8. Composite georeferenced image of the infrared and high-resolution imagery products collected from MASS in the Gulf of Mexico on 30 Oct 2011 during the crossing of a sharp temperature front at the northern edge of the Loop Current. Note the enhanced wave breaking (small white features) on the southern, warmer side of the temperature front.

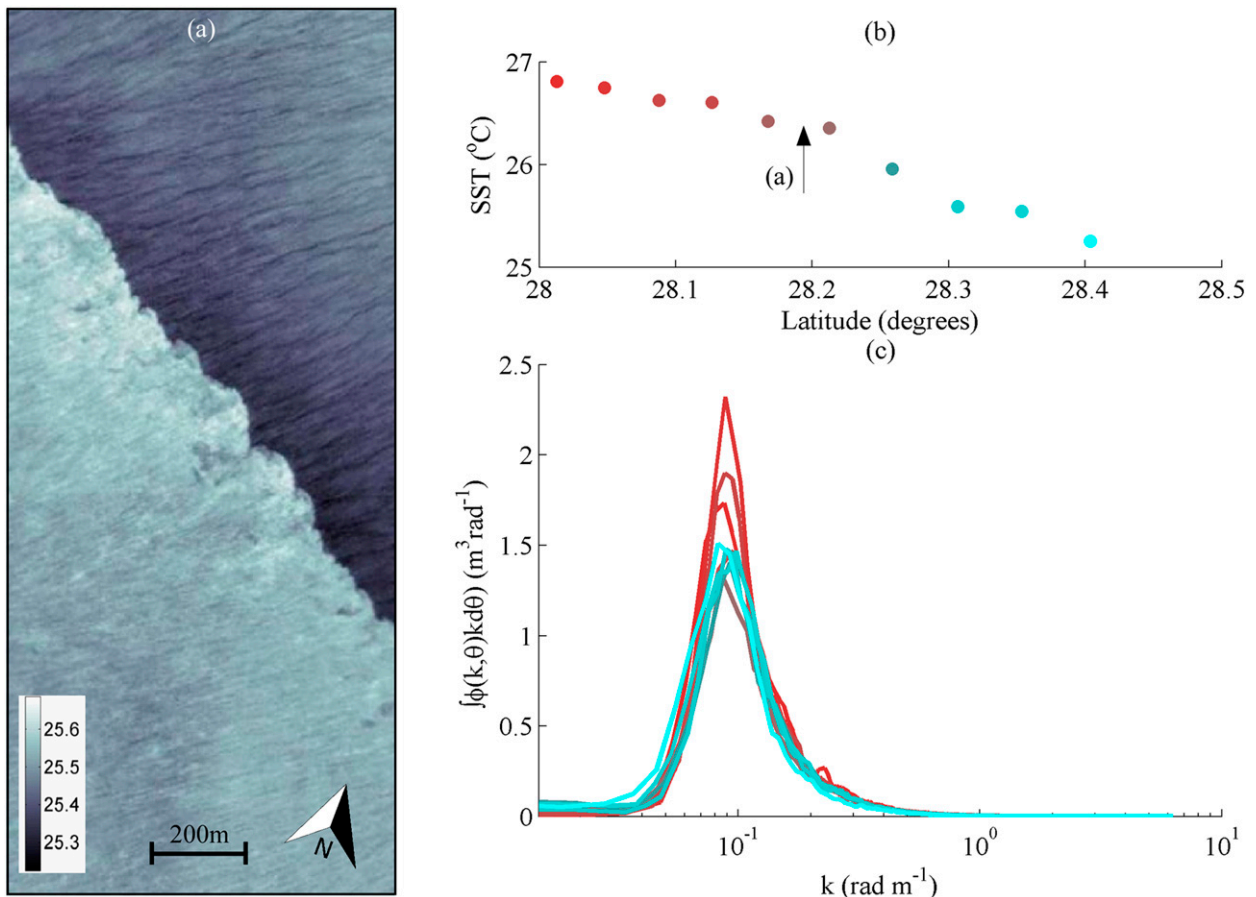


FIG. 9. (a) SST imagery of the northern edge of the Loop Current on 30 Oct 2011. Note the linear features aligned in the northeast-southwest direction. These are believed to be the surface signatures of Langmuir circulation (or Langmuir turbulence) that are approximately aligned with the wind and the direction of dominant wave propagation. (b),(c) Evolution of the omnidirectional wavenumber spectrum as the aircraft flew across the Loop Current. The color scale represents the average SST over the length of the wave record (4 km) used in the spectral analysis, also shown as a function of latitude in (b).

inferred Stokes drift) and the surface temperature field will prove important in remote sensing of these upper-ocean processes.

d. SSHA from airborne and satellite altimetry

The MASS lidar altimetry data from the flight shown in Fig. 6 were averaged across the swath width (250–500 m depending on flight altitude) and were corrected for solar and lunar ocean tides using the FES2004 model of the solid earth tides (McCarthy and Petit 2004), the pole tides, and other tidal loading corrections (FES2004).

With these corrections the comparison between the *Jason-1* SSH and SSH anomaly (SSHA) are shown in Fig. 10 over the part of the track extending from latitudes of approximately 28° to 29.75°N, with the lidar data averaged over a $\Delta\text{lat} = 0.05^\circ$. At this resolution the rms error between the satellite and lidar data is a few centimeters. However, as shown in Fig. 11, when the lidar data are averaged over a $\Delta\text{lat} = 0.005^\circ$, it becomes

apparent that improved agreement between the two sets of data is achieved, implying that the lower-resolution data are not sufficient to include the higher-wavenumber signals in the SSHA. A brief consideration of the bathymetry under the flight track (also shown in Fig. 11) suggests that these data may include the surface signatures of internal waves generated on the continental slope (Helfrich and Melville 2006), although we have no in situ measurements to confirm this hypothesis.

The comparison of the SWH ($4 \times$ rms surface displacement) measured by *Jason-1* and the lidar is also shown in Fig. 12. Generally, the differences are less than 10 cm with the largest being in the range of 20–25 cm within approximately 50 km of the coast.

e. Hyperspectral imagery of the ocean surface and nearshore transport

The hyperspectral imager in MASS permits the measurement of the near-surface concentration of

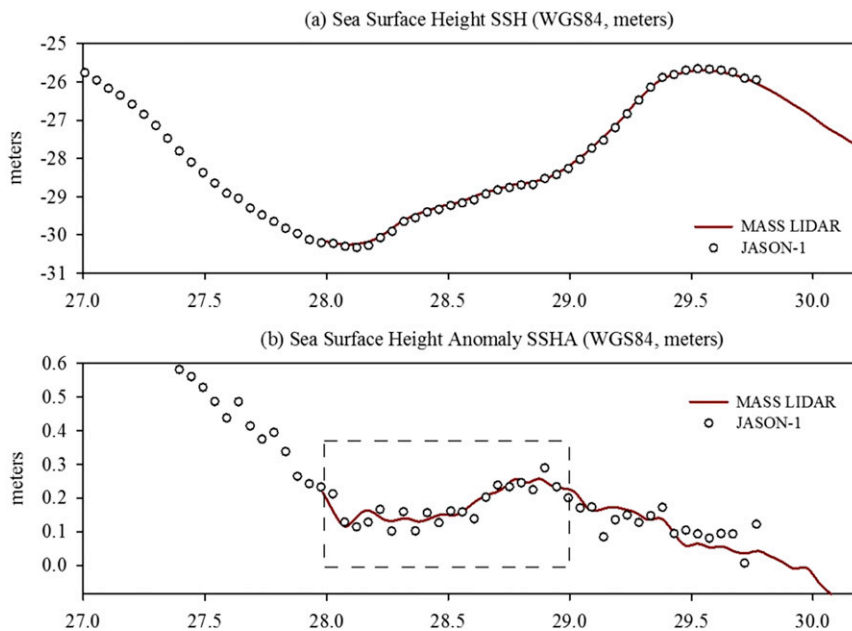


FIG. 10. SSH, SSHA vs latitude ($^{\circ}$ N) measured from *Jason-1* satellite altimeter, and the MASS lidar. The dashed rectangle shows the location of the subset of data plotted in Fig. 11.

phytoplankton pigments, such as chlorophyll-*a* (Chl-*a*), which is an index of phytoplankton biomass. Chl-*a* is associated with ocean productivity through photosynthesis by phytoplankton in the near-surface layer of the ocean (O'Reilly et al. 1998). While Chl-*a* is common in most phytoplankton, other pigments can be used to identify different phytoplankton species or functional groups. Differentiating between phytoplankton groups and/or size classes is important as these groups have different characteristics that affect their impact on the global carbon cycle, the biological pump, and trophic interactions. Detecting phytoplankton functional groups (PFTs) from space is therefore a major challenge for new and planned satellite sensors (Bracher et al. 2015). Figure 13 shows MASS hyperspectral imagery of La Jolla Bay, California, coastal waters near Scripps Pier during a red tide event that was caused by high concentrations of a dinoflagellate *Lingulodinium polyedrum*. *Lingulodinium* blooms are known to occur in this area and have high absorption in the ultraviolet part of the spectrum (Kahru and Mitchell 1998) due to the presence of mycosporine-like amino acids. The planned next-generation NASA ocean missions Pre-Aerosol, Clouds, and Ocean Ecosystem (PACE) and Hyperspectral Infrared Imager (HyspIRI) will have close to hyperspectral characteristics with 5–10-nm resolution but with lower spatial resolution. MASS images show highly resolved spatial and spectral features that are not possible to obtain with current spaceborne

instruments. Data were collected over 246 bands (407–985 nm) with a spatial resolution of 0.5–2 m. The inset shows the spectra at locations A and B on the aerial image, demonstrating the influence of the dinoflagellates on hyperspectral reflectance. The drastic change in reflectance spectra depending on the concentration of dinoflagellates demonstrates the value of hyperspectral measurements. However, a spaceborne sensor with ground resolution of about 1 km will not be able to resolve the small-scale features and will have smeared spectra. Note the large changes in the spectra over scales of $O(100)$ m and less. The implication of these data is that in conducting physical-biogeochemical modeling of red tides and related processes of intermittent phytoplankton blooms, subgrid-scale modeling will be required to account for these very small-scale processes that ultimately proceed at the molecular scale. Datasets like those shown in Fig. 13 will be valuable for algorithm development and interpretation of lower-resolution images from spaceborne sensors.

In addition to monitoring ocean biology, the hyperspectral imager has also been used to trace dyes in experiments on transport in nearshore flows. Figure 14 shows a sequence of images of the along-shore transport and dispersion of a fluorescent dye (rhodamine WT) introduced at the mouth of the New River Inlet in May 2012 (Clark et al. 2014). It is shown as the surface concentration of the dye through measurements over the 530–610-nm range of the imager.

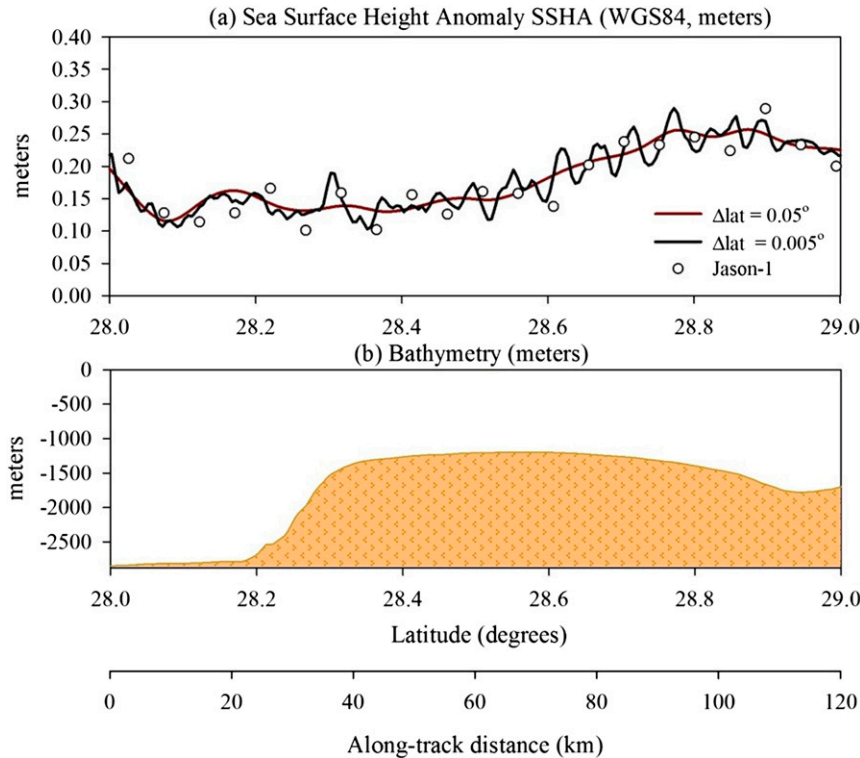


FIG. 11. (a) SSHA estimated from the MASS lidar for two averaging lengths, 0.05° and 0.005° . (b) Bathymetry under the flight track. Note the presence of surface signatures of lengths 5–10 km north of the break in the shelf.

These data were favorably compared with in situ measurements made from a personal watercraft. With the impact of coastal pollution on the ecology and the economics of the coastal environment through the closing of beaches, the ability to use airborne measurements to test coastal models and rapidly track pollution is a very useful application of MASS. The ability to combine the dye measurements with wave and current measurements of the kind described above will contribute to advancing our understanding of nearshore processes.

4. Applications in the terrestrial and built environment

There are numerous applications for MASS-like multi-instrument systems in the terrestrial and built environment and their full coverage is beyond this paper; however, we have used MASS, and a similar system, to undertake exploratory studies in the areas of snowpack measurement and urban remote sensing.

a. Sierra Nevada snowpack measurements

Lidar is increasingly recognized as an important tool for addressing some of the challenges in measuring the

hydrological cycle and water-related infrastructure. Lidar surveys can be an invaluable tool to augment traditional point measurements. In California, applications include watershed flood monitoring, the state of the aging and failing levees along the major rivers and in the Sacramento–San Joaquin Rivers delta estuary, and quantifying and understanding the storage and melt of water in the snowpack. In spring 2011, a combination of

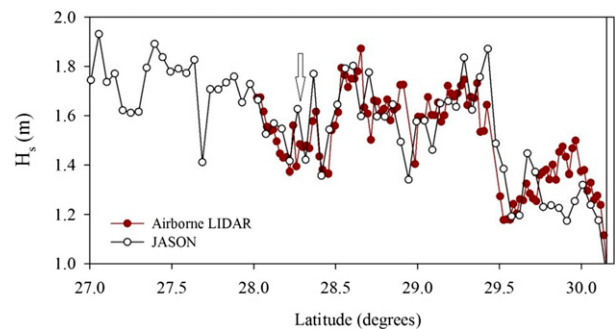


FIG. 12. Comparison of SWH measured by *Jason-1* and the MASS lidar. The largest differences occur within 50 km of the Gulf Coast at the right of the figure. Note that the vertical arrow marks the region of the northern frontal boundary of the Loop Current showing an increase in the SWH as the dominant waves propagate from the northeast across the front (see Fig. 9).

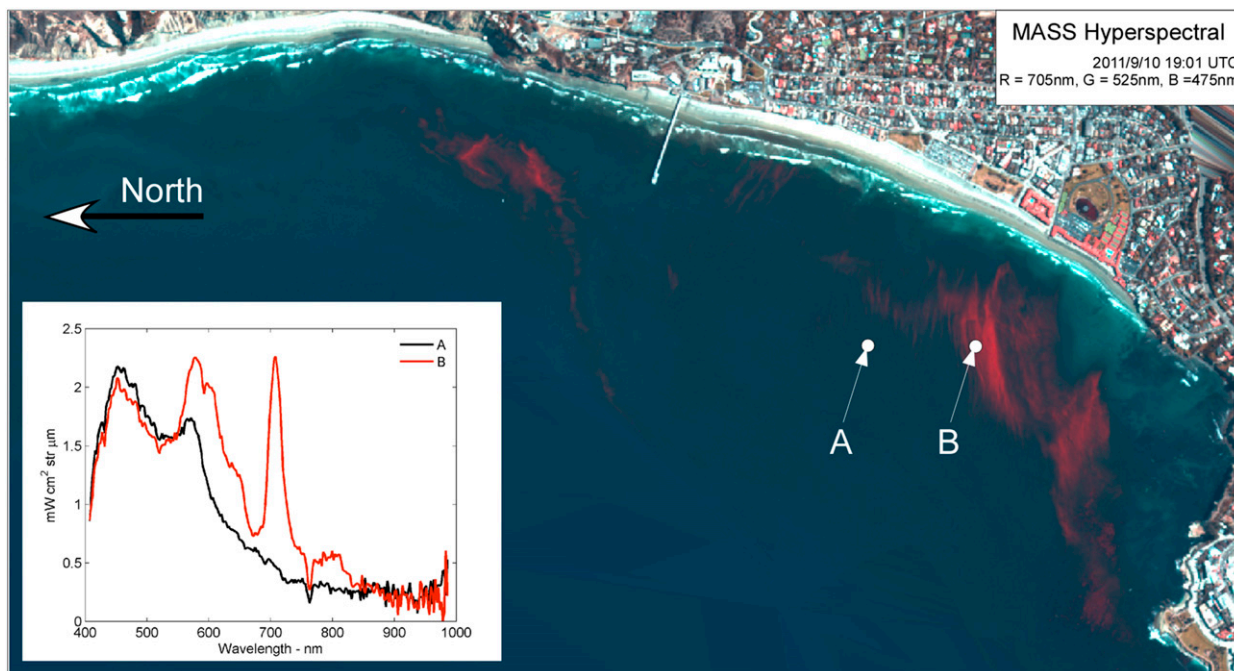


FIG. 13. Aerial hyperspectral imagery of the La Jolla coastal waters during a red tide event (dinoflagellate bloom). Data were typically collected over 246 bands (407–985 nm) with spatial resolution of 0.5–2 m. The inset shows the spectra at A and B.

airborne and terrestrial lidars was used to observe the spatially complex and temporally dynamic structure of snow depth within the American River watershed of the central Sierra Nevada region.

Flights during snow-laden and bare-ground periods were carried out using the MASS airborne lidar system. The experimental flights were made at approximately 1000 m above ground level, obtaining lidar swath widths of approximately 1000 m in a star flight pattern that covered a swath of approximately 50 km long by 1.5 km wide in both the west–east and north–south directions centered above the Central Sierra Snow Laboratory (CSSL) at the crest of the Sierra Nevada in Donner Pass near Truckee, California, along the Interstate 80 corridor. The airborne lidar observations achieved sample horizontal resolutions of 1–1.5 m with expected vertical positions accurate to 5 cm or less.

Complementing the airborne lidar surveys, a terrestrial scanning lidar was installed at the CSSL approximately 2 km west of Donner Pass (Fig. 15). This portable system, a Riegl Q240i, was installed to continuously monitor a snow-covered landscape from the CSSL over a several-day period that straddled the airborne lidar survey on 12 May 2011. The lidar was mounted in the CSSL facility looking out a window overlooking the adjacent meadow and forested area. It scanned a vertical arc of $\pm 40^\circ$ for 40 s within a 50° angle sweep at $1/2^\circ$ increments every 100 min. The resulting observations

provided a record of the snow surface near the CSSL from 7 to 22 May 2011. The lidar recorded snow accumulations of approximately 40 cm between 14 and 18 May but, in general, these 3 weeks were a period of declining snow depth that resulted in approximately 10 cm of snow surface decline per day. The lidar observations were in close agreement with nearby measurements of snow depth from an acoustic snow sensor.

b. The built environment

There is great interest in the radiative and thermal properties of the built environment in order to understand the urban heat island effect. Generally, the albedo of the urban fabric is smaller than that of the surrounding natural area. This has diverse impacts, ranging from the accelerated aging of road pavements and roofs to heating of the urban atmospheric boundary layer that reduces human comfort and increases building cooling energy use. Large-scale albedo and surface temperature changes can be resolved by satellites, but MASS overflights generate building-resolving products over a wide range of wavelengths. Figure 16c shows strong variations in the spectral reflectance between grass and concrete, suggesting that narrow single-spectral-band measurements are not sufficient for accurate albedo measurements. Such data could also be used to analyze the aging of reflective roof coatings or dirt built up on solar photovoltaic panels.

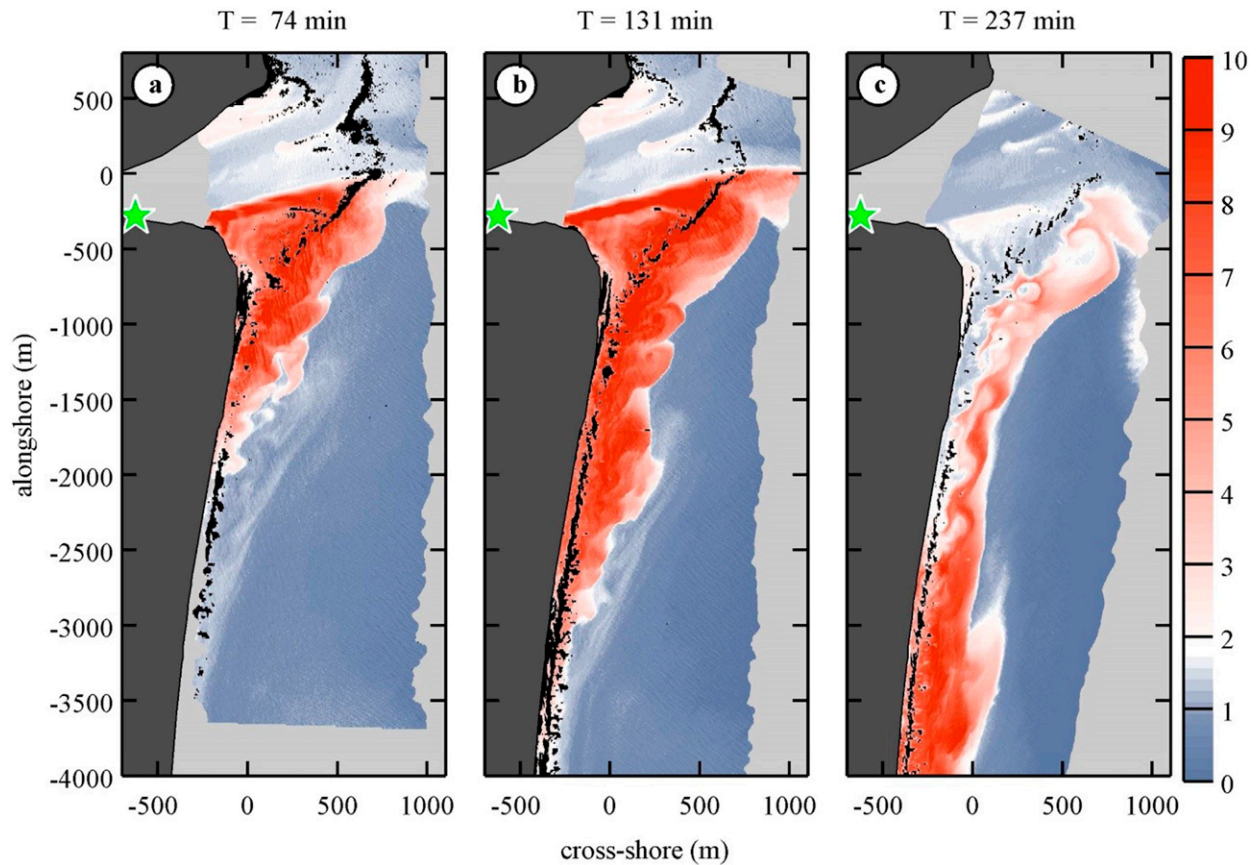


FIG. 14. Example of aerial hyperspectral imagery of rhodamine WT dye released at the mouth of New River inlet collected on 7 May 2012 during the ONR RIVET DRI, shown as estimated dye concentration (ppb). (From Clark et al. 2014.)

Reflective roof coatings are designed to be highly reflective across the solar spectrum, but aging due to UV irradiation and pollution significantly reduces reflectivity in the aged state. Modelers will also appreciate the richness of MASS data for automated land-cover classification, and digital elevation model and vegetation representation (Figs. 16b,d)

for building-resolving urban fluid flow, thermal radiation, and dispersion simulations.

5. Discussion

This survey of airborne measurements, using the suite of instruments included in MASS, demonstrates that

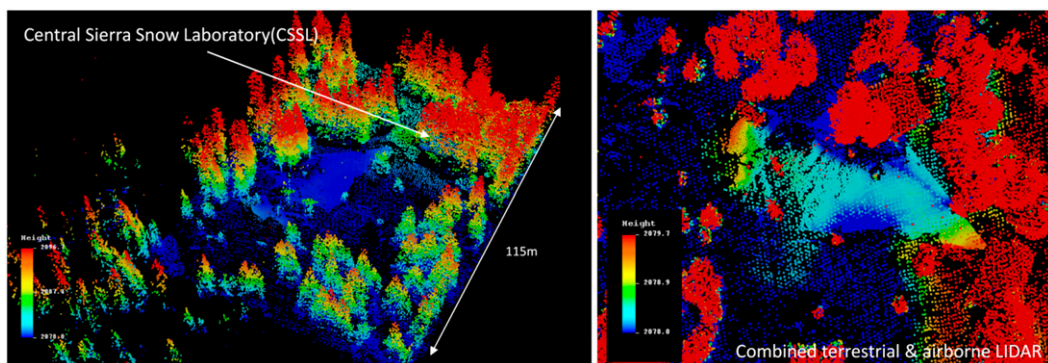


FIG. 15. Snow elevation measurements at the CSSL in the Sierra Nevada during winter 2010/11 using terrestrial and airborne lidar (Riegl Q240i and Q680i, respectively).

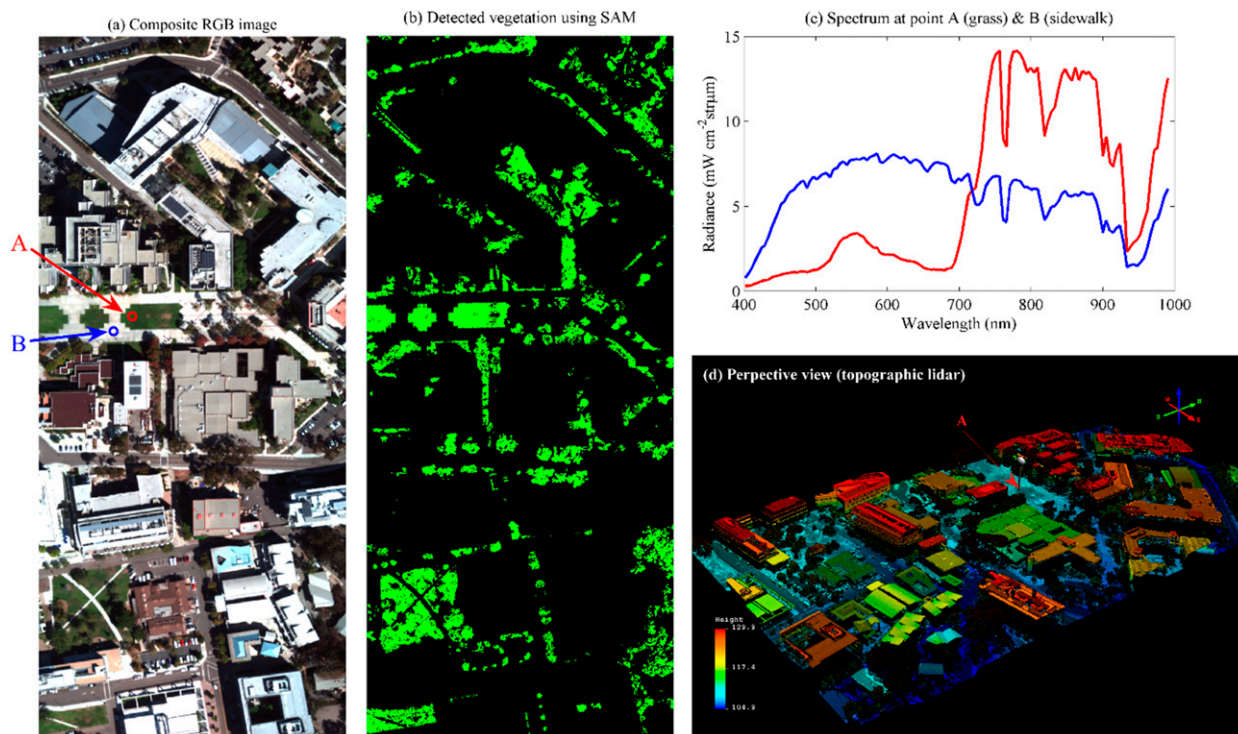


FIG. 16. (a) Composite red–green–blue (RGB) image (red: 632.03 nm; green: 533.86 nm; blue: 465.12 nm) of part of the University of California, San Diego (UCSD), campus collected from the MASS hyperspectral imager on 26 Sep 2014. (b) Detected vegetation using standard spectral angle mapper (SAM) classification, matching the vegetation spectrum at point A in (a). (c) Spectra of points A (grass) and B (sidewalk) in (a). (d) Perspective view, with color-coded elevation, of the same area of the UCSD campus collected from the MASS topographic lidar during the same flight.

they can be important tools for broadband micro- to mesoscale measurements of ocean surface processes. Airborne lidar-based altimetry and supporting visible and IR imaging can be used to measure processes having response times much shorter than the typical repeat cycle of satellite altimetry. Being portable for deployment on a variety of aircraft makes MASS amenable for use in rapid-response applications (e.g., storm surges, extreme waves, hurricanes, tsunamis, floods, avalanches, and mudslides).

Furthermore, MASS-type systems can play a significant role in satellite mission and instrument design, and in testing and calibration–validation of satellite remote sensing instruments over a range of electromagnetic wavelengths and phenomena, including physical, chemical, and biological processes. For example, it is expected that such systems could significantly complement the development and testing phases of the Surface Water and Ocean Topography (SWOT) mission of CNES and NASA.

More specifically, the data presented here clearly show that the surface wave field is modulated by surface current gradients, as is to be expected from geometrical optics or Wentzel–Kramers–Brillouin (WKB) theory. This has important implications for high-resolution

satellite remote sensing of sea surface topography as it approaches the scales of surface-wave effects.

The applications in hydrology and studies of the built environment are only touched on here, but they give some sense of the breadth of uses of MASS, its precision, and resolution for use in those fields.

It must be emphasized that this is a technology paper, so while we have presented many examples of the uses of MASS, we have not gone into great detail on the physical processes underlying the measurements. This will be left to scientific papers.

Acknowledgments. This research was funded by an NSF MRI (ARRA) grant to WKM, DC, MK, Robert Guza, and Paul Linden at SIO/UCSD for most of the MASS instruments and system development for application to oceanographic, hydrographic and built-environment research. It was also supported by an industry grant to WKM for the October 2011 GoM experiment, and by the Basker Chair Fund for PFL. The collection of other data used here was funded by grants to WKM by ONR (Physical Oceanography). The authors are grateful to Aspen Helicopter for providing flight resources and to Bradley Busch for his excellent piloting during the GoM flights.

REFERENCES

- Banner, M. L., 1990: Equilibrium spectra of wind waves. *J. Phys. Oceanogr.*, **20**, 966–984, doi:10.1175/1520-0485(1990)020<0966:ESOWW>2.0.CO;2.
- Bracher, A., and Coauthors, 2015: Report on IOCCG workshop: Phytoplankton composition from space; Towards a validation strategy for satellite algorithms. NASA Tech. Memo. NASA/TM-2015-217528, 40 pp.
- Clark, D. B., L. Lenain, F. Feddersen, E. Boss, and R. T. Guza, 2014: Aerial imaging of fluorescent dye in the near shore. *J. Atmos. Oceanic Technol.*, **31**, 1410–1421, doi:10.1175/JTECH-D-13-00230.1.
- Hanley, K. E., S. E. Belcher, and P. P. Sullivan, 2010: A global climatology of wind–wave interaction. *J. Phys. Oceanogr.*, **40**, 1263–1282, doi:10.1175/2010JPO4377.1.
- Helfrich, K. R., and W. K. Melville, 2006: Long nonlinear internal waves. *Annu. Rev. Fluid Mech.*, **38**, 395–425, doi:10.1146/annurev.fluid.38.050304.092129.
- Huang, Z.-C., B. D. Reineman, L. Lenain, W. K. Melville, and J. H. Middleton, 2012: Airborne lidar measurements of wave energy dissipation in a coral reef lagoon system. *J. Geophys. Res.*, **117**, C03016, doi:10.1029/2011JC007203.
- Kahru, M., and B. G. Mitchell, 1998: Spectral reflectance and absorption of a massive red tide off southern California. *J. Geophys. Res.*, **103**, 21 601–21 609, doi:10.1029/98JC01945.
- Kenyon, K. E., 1969: Stokes drift for random gravity waves. *J. Geophys. Res.*, **74**, 6991, doi:10.1029/JC074i028p06991.
- Kleiss, J. M., and W. K. Melville, 2010: Observations of wave breaking kinematics in fetch-limited seas. *J. Phys. Oceanogr.*, **40**, 2575–2604, doi:10.1175/2010JPO4383.1.
- , and —, 2011: The analysis of sea surface imagery for whitecap kinematics. *J. Atmos. Oceanic Technol.*, **28**, 219–243, doi:10.1175/2010JTECHO744.1.
- Lee, Z. P., J. Marra, M. J. Perry, and M. Kahru, 2015: Estimating oceanic primary productivity from ocean color remote sensing: A strategic assessment. *J. Mar. Syst.*, **149**, 50–59, doi:10.1016/j.jmarsys.2014.11.015.
- Liu, C., 2009: Beyond pixels: Exploring new representations and applications for motion analysis. Ph.D. thesis, Massachusetts Institute of Technology, 164 pp.
- Marmorino, G. O., G. B. Smith, J. V. Toporkov, M. A. Sletten, D. Perkovic, and S. J. Frasier, 2008: Evolution of ocean slicks under a rising wind. *J. Geophys. Res.*, **113**, C04030, doi:10.1029/2007JC004538.
- McCarthy, D. D., and G. Petit, Eds, 2004: IERS conventions (2003). IERS Tech. Note 32, 127 pp.
- Mei, C. C., M. Stiassnie, and D. K.-P. Yue, 2005: *Theory and Applications of Ocean Surface Waves: Part 2; Nonlinear Aspects*. Advanced Series on Ocean Engineering, Vol. 23, World Scientific, 1071 pp.
- Melville, W. K., and P. Matusov, 2002: Distribution of breaking waves at the ocean surface. *Nature*, **417**, 58–63, doi:10.1038/417058a.
- NASA, 2008: Jason-1 Altimeter Geophysical Data Record (GDR) NetCDF. Version 1, PO.DAAC, accessed 11 March 2016. [Available online at https://podaac.jpl.nasa.gov/dataset/JASON-1_GDR_NETCDF.]
- , 2014: Moderate-resolution Imaging Spectroradiometer (MODIS) Terra Ocean Color Data, 2014 reprocessing. OB.DAAC, accessed 11 March 2016, doi:10.5067/TERRA/MODIS_OC.2014.0.
- O'Reilly, J. E., S. Maritorena, B. G. Mitchell, D. A. Siegel, K. L. Carder, S. A. Garver, M. Kahru, and C. McClain, 1998: Ocean color chlorophyll algorithms for SeaWiFS. *J. Geophys. Res.*, **103**, 24 937–24 953, doi:10.1029/98JC02160.
- Phillips, O. M., 1985: Spectral and statistical properties of the equilibrium range in wind-generated gravity waves. *J. Fluid Mech.*, **156**, 505–531, doi:10.1017/S0022112085002221.
- Reineman, B. D., L. Lenain, D. Castel, and W. K. Melville, 2009: A portable airborne scanning lidar system for ocean and coastal applications. *J. Atmos. Oceanic Technol.*, **26**, 2626–2641, doi:10.1175/2009JTECHO703.1.
- Romero, L., and W. K. Melville, 2010a: Airborne observation of fetch-limited waves in the Gulf of Tehuantepec. *J. Phys. Oceanogr.*, **40**, 441–465, doi:10.1175/2009JPO4127.1.
- , and —, 2010b: Numerical modeling of fetch-limited waves in the Gulf of Tehuantepec. *J. Phys. Oceanogr.*, **40**, 466–486, doi:10.1175/2009JPO4128.1.
- , —, and J. M. Kless, 2012: Spectral energy dissipation due to surface wave breaking. *J. Phys. Oceanogr.*, **42**, 1421–1444, doi:10.1175/JPO-D-11-072.1.
- Ryu, J.-H., H.-J. Han, S. Cho, Y.-J. Park, and Y.-H. Ahn, 2012: Overview of geostationary ocean color imager (GOCI) and GOCI data processing system (GDPS). *Ocean Sci. J.*, **47**, 223–233, doi:10.1007/s12601-012-0024-4.
- Sutherland, P., and W. K. Melville, 2013: Field measurements and scaling of ocean surface wave-breaking statistics. *Geophys. Res. Lett.*, **40**, 3074–3079, doi:10.1002/grl.50584.
- Vierling, K. T., L. A. Vierling, W. A. Gould, S. Martinuzzi, and R. M. Clawges, 2008: Lidar: Shedding new light on habitat characterization and modeling. *Front. Ecol. Environ.*, **6**, 90–98, doi:10.1890/070001.